Arctic seafloor methane seepage since the Last Glacial Maximum

Schneider, A.[1], Panieri, G.[1], Lepland, A.[1,2,8], Consolaro, C.[1,3], Crémière, A.[2, 4*], Forwick, M.[5], Johnson, J.E.[6], Plaza-Faverola, A.[1], Sauer, S.[1,2,7*], Knies, J.[1,2]

[1] CAGE – Centre for Arctic Gas Hydrate, Environment and Climate, UiT The Arctic University of Norway, Department of Geosciences, 9037 Tromsø, Norway

[2] Geological Survey of Norway, 7491 Trondheim, Norway

[3] School of Geography, Earth & Environmental Sciences, Plymouth University, Drake Circus, Plymouth PL4 8AA, UK

[4] Division of Geological and Planetary Sciences, California Institute of Technology, Pasadena, California, USA

[5] Department of Geosciences, UiT The Arctic University of Norway, 9037 Tromsø, Norway

[6] Department of Earth Sciences, University of New Hampshire, Durham, NH, USA

[7] Institut Français de Recherche pour l'Exploitation de la Mer (Ifremer), Department of Marine Geosciences, Plouzané, France

[8] Department of Geology, Tallinn University of Technology, Tallinn, Estonia

* Current affiliation

Abstract

Multiple proxies in the geological record offshore NW Svalbard track shallow subseafloor diagenesis and seafloor methane seepage during the Last Glacial Maximum (LGM) extent and disintegration of the Svalbard Barents Sea Ice Sheet (SBIS). Vestnesa Ridge, located at 79°N in 1200 m water depth, is one of the northernmost known active methane seep sites and is characterised by a subseafloor fluid flow system, numerous seafloor pockmarks and gas flares in the water column. In this study, we develop a Late Pleistocene and Holocene stratigraphic framework, use stable oxygen and carbon isotope signatures ($\delta^{18}O$, $\delta^{13}C$) of benthonic and planktonic foraminifera, the mineralogical and carbon isotope composition of methane-derived authigenic carbonate (MDAC), and sediment geochemical data of ten sediment cores to assess methane seepage variability on Vestnesa Ridge.

The studied cores record 32 negative $\delta^{13}C$ excursions in benthonic and planktonic foraminifera with amplitudes down to -29‰ VPDB. These $\delta^{13}C$ excursions are often associated with elevated Ca/Ti and Sr/Ti elemental ratios in sediments, and methane-derived authigenic carbonate nodules. The precipitation of MDAC overgrowths on foraminiferal tests drives most of the negative $\delta^{13}C$ excursions. In this dataset, the oldest recorded methane emission episodes on Vestnesa Ridge occurred during the LGM (24-23.5 cal ka BP), and during Heinrich Event 1 (HE 1; 17.7-16.8 cal ka BP).

Geological indicators for past subseafloor methane cycling and seafloor methane seepage, such as negative foraminiferal $\delta^{13}C$ excursions, MDAC nodules, and elevated Sr/Ti elemental ratios recorded in post-LGM sediments, possibly represent vertical migration of the sulphate-methane transition zone (SMTZ) and post-date sedimentation by up to 13.4 ka. However, it is important to note that indications of post-LGM seafloor methane seepage at Vestnesa Ridge also correspond to the established methane efflux chronology for the adjacent Barents Sea shelf, implying that glacio-isostatic adjustments and associated re-activation of pre-existing deep-seated faults after disintegration of the SBIS are likely the main controlling factors for the fluid migration towards the seafloor at Vestnesa Ridge.

Keywords (categories demanded by QSR are underlined)

Micropaleontology, Foraminifers, Stable isotopes, Methane seepage, Authigenic carbonate, Holocene, Pleistocene, Paleogeography, Deglaciation, Arctic Ocean

Highlights

- Multiple proxies document methane seepage from Vestnesa Ridge since the LGM.
- Diagenetic alteration and MDAC precipitation may postdate the host sediment age by up to 13.4 ka.
- Timing of methane seepage corresponds to the LGM and deglaciation of the SBIS.
- Glacio-isostatic adjustments may be a key control on methane seepage.

1 Introduction

Current global warming raises concern about the role of methane, a powerful greenhouse gas, in the Arctic (IPCC, 2013; AMAP, 2015) as the circum-Arctic is expected to experience a larger temperature increase than any other region on the planet (Serreze and Barry, 2011; IPCC, 2013; AMAP, 2015). In the upcoming century, increasing Arctic bottom water temperatures are hypothesised as potential drivers for destabilisation of gas hydrates along continental margins that may cause unprecedented release of methane into the water column and the atmosphere (Reagan and Moridis 2007; Biastoch et al., 2011; Giustiniani et al., 2013; Kretschmer et al., 2015; James et al., 2016). Although causal relationships between recent climate warming and increased methane release from Arctic Ocean sediments may seem likely, seepage observed today could have been initiated thousands of years ago. For example, methane release on the East Siberian Arctic Shelf attributed to current global warming (Shakhova et al., 2010) is more likely the result of submarine permafrost thaw after the inundation of

terrestrial permafrost during the Holocene marine transgression (Bauch et al. 2001a; Dmitrenko et al., 2011).

To evaluate if climate warming or other Earth system processes affect the release of methane stored in Arctic Ocean sediments, a better understanding of the timing and drivers of past methane seepage variability in the Arctic is required. Since active methane seepage at Vestnesa Ridge, western Svalbard (Fig. 1), was documented in water column acoustic data, research in the area has provided key information for understanding the dynamics of seafloor methane release and seepage driving mechanisms over geological time scales in Arctic regions (Panieri et al. 2017b and references therein). Previous studies found evidence for seepage occurring during the past 17 cal ka (Panieri et al., 2014; Consolaro et al., 2015; Ambrose et al., 2015; Sztybor and Rasmussen, 2017a; 2017b; Schneider et al., 2017). However, these observations have limited regional coverage. The objective of this study is to identify events of past methane seepage along the approximately 100 km long Vestnesa Ridge since the Last Glacial Maximum (LGM) and during the retreat of the Svalbard-Barents Sea Ice Sheet (SBIS). We develop a Late Pleistocene and Holocene stratigraphic framework for the investigated sediment cores from Vestnesa Ridge, and correlate our sedimentary record with established stratigraphic marker horizons along the western Svalbard continental margin. We use multiple proxies such as $\delta^{18}O$ and $\delta^{13}C$ records from benthonic and planktonic foraminifera, chemosynthetic bivalves, mineralogy and $\delta^{13}C$ of MDAC, and sediment geochemical data to identify shallow subseafloor diagenetic methane cycling and seafloor methane seepage. This study provides the first comprehensive insight into timing and drivers of methane seepage activity or quiescence along Vestnesa Ridge since the LGM.

2 Background and processes in gas-charged sediments

Methane (CH_4) can be of microbial, thermogenic, or abiotic origin (Whiticar, 1999) and occurs in hydrocarbon reservoirs, stored in hydrate, or as dissolved and free gas in continental margin sediments worldwide (Kretschmer et al., 2015; Ruppel et al., 2017). The zone within the sediment column where gas hydrates are stable is known as gas hydrate stability zone (GHSZ) and is primarily determined by

specific temperature and pressure conditions (Sloan, 1998; Kvenvolden, 1998). When temperature increases and/or pressure decreases, gas hydrates dissociate and fluids, including free gas, can be released. Methane seepage occurs where fluids enriched in methane migrate toward the sediment-water interface (e.g. Torres and Bohrmann, 2006; Etiope, 2015). Seepage is commonly understood as the release of fluids from the seafloor on continental margins (in pockmarks) and its location is named "seep" (Judd and Hovland, 2007 and references therein).

The geochemical conditions at methane seeps are characterised by opposing gradients of porewater sulphate (SO_4^{2-}) and methane. A biogeochemical zone within near-surface sediments (within centimetres or metres), the sulphate-methane transition zone (SMTZ), establishes where microbial co-metabolism counterbalances the upward flux of methane and the downward flux of sulphate into shallow sediments (Reeburgh, 1976; Whiticar and Faber, 1986; Valentine, 2002; Tryon, et al. 1999). A changing methane flux can cause vertical migration of the SMTZ through the sediment (Borowski et al., 1996). A key geochemical process at the SMTZ (Eq. 1) is the microbially mediated anaerobic oxidation of methane (AOM) involving syntrophic consortia of methane-oxidizing archaea and sulphate-reducing bacteria (Knittel and Boetius, 2009 and references therein):

$$CH_4 + SO_4^{2-} \rightarrow HCO_3^- + HS^- + H_2O \qquad \text{(Eq. 1)}$$

Reducing conditions at the SMTZ can result in reductive dissolution of magnetic Fe-oxides (Canfield and Berner, 1987; Peckmann et al., 2001; Riedinger et al., 2005; Novosel et al., 2005; Dewangen et al., 2013) and alteration of the initial sediment composition and magnetic properties due to replacement of magnetic Fe-oxides by paramagnetic authigenic Fe-sulfides (Ferrell and Aharon, 1994; Bohrmann et al., 1998; Rodriguez et al., 2000; Greinert et al., 2001; März et al., 2008; Lin et al., 2016; 2017). Barium (Ba^{2+}) that is present dissolved in seep fluids (Hanor, 2000; Torres et al., 2003a) can react with porewater sulphate and can precipitate as authigenic barite ($BaSO_4$) at the upper boundary of the SMTZ (Torres et al., 1996, Dickens, 2001; Paytan et al., 2002; Riedinger at el., 2006; Kasten et al., 2012;

Sauer et al., 2017). As porewater sulphate is depleted underneath the SMTZ, buried barite dissolves and barium diffuses upward to the SMTZ where it re-precipitates as authigenic barite (Torres et al., 1996; Dickens, 2001). Barite fronts are commonly found immediately above the present-day depth of porewater sulphate depletion (Dickens, 2001; Riedinger et al., 2006) and serve as a geochemical tracer of the SMTZ.

The SMTZ is also the sedimentary interval where MDAC precipitate, and subseafloor diagenesis occurs at and near the SMTZ. The AOM (Eq. 1) elevates the porewater alkalinity (Ritger et al., 1986; Paull et al., 1992), and thus promotes the precipitation of $Ca(Mg/Sr)CO_3$ (Eq. 2):

$$2\ HCO_3^- + Ca^{2+}\ (Mg^{2+}/Sr^{2+}) \rightarrow Ca(Mg/Sr)CO_3 + CO_2 + H_2O \qquad \text{(Eq. 2)}$$

Carbonates with $\delta^{13}C$ values more negative than -30‰ VPDB are consistent with carbon sourced from anaerobic microbial oxidation of methane (Whiticar, 1999; Aloisi et al., 2000; Bohrmann et al., 2001; Greinert et al., 2001; Naehr et al., 2007). MDACs are often composed of aragonite, high-Mg calcite (5-20mol% $MgCO_3$, Burton 1993), or dolomite (Bohrmann et al., 1998; 2001; Aloisi et al., 2000; Greinert et al., 2001, Naehr et al., 2007) and occur as early diagenetic micrite-cemented nodules, cavity fills, coatings, or crusts on the seafloor (Bohrmann et al., 1998; 2002; Mazzini et al., 2004; Bayon et al., 2009; Crémière et al., 2016a; Sauer et al., 2017). Aragonite and high-Mg calcite precipitate near the seafloor and indicate that the SMTZ was located in the shallow subsurface (cm or dm scale) at high CH_4-flux (Aloisi et al., 2000; Greinert et al., 2001; Naehr et al., 2007). Savard (1996) suggested micrite-cemented nodules can precipitate *in-situ*, whereas large MDAC crusts require time spans of hundreds to thousands of years to form and often yield different ages compared to their host sediment (Teichert et al., 2003; Bayon et al., 2009; Luff et al., 2004; 2005).

Together with fossil remains of seep fauna, MDACs provide direct geological evidence of AOM and methane seepage in the sedimentary record. Panieri et al. (2017a) showed that foraminifera serve as preferred nucleation templates for authigenic Mg-calcite at methane seepage sites. Negative $\delta^{13}C$

148 excursions from benthonic foraminifera in sediment core records have been used to identify periodic
149 release of methane stored in gas hydrates at various times in earth history (Dickens, 1997; Kennet et
150 al., 2000; Thomas et al., 2002; Jenkyns et al., 2003; Tripati and Elderfield, 2005; Zachos et al., 2007).
151 Several studies have shown that MDAC precipitates form coatings around foraminiferal tests, and may
152 overprint the primary shell mineralogy and stable isotope composition, which complicates the use of
153 foraminiferal $\delta^{13}C$ records as past seepage archives (Rathburn et al. 2000; Torres et al., 2003b; 2010;
154 Martin et al., 2010; Panieri et al., 2009; 2014; 2017a; Consolaro et al., 2015; Schneider et al., 2017).
155

156 ## 3 Study area

157 Vestnesa Ridge is located at 79°N on the western continental margin of the Svalbard Archipelago (Fig.
158 1 a; b). The ridge, in 1200-1300m water depth, is approximately 100 km long and composed of >2 km
159 thick Pliocene and Pleistocene sediments overlying < 20 Ma old oceanic crust (Eiken and Hinz, 1993;
160 Engen et al., 2008). The youngest sediments, of Late Pleistocene and Holocene age, are silty turbidites,
161 muddy-silty contourites and hemipelagites (Vogt et al., 1994; 1999; Howe et al., 2008).
162 Up to 900 m high gas flares probably emit a mixture of microbial and thermogenic gas (Smith et al.,
163 2014; Panieri et al., 2017b). A Bottom Simulating Reflector (BSR) located ~160–180 m bsf (meters
164 below seafloor) as well as an underlying zone of high amplitudes and anomalous low seismic velocities
165 indicate the presence of free gas at the base of the GHSZ (Petersen et al., 2010; Goswami et al., 2015;
166 Plaza-Faverola et al., 2015). Vertical fluid flow conduits (chimneys) cross the BSR, intersect the
167 overlying sediments, connect to the seafloor at pockmarks, and thus allow vertical fluid migration
168 (Petersen et al., 2010; Bünz et al., 2012). Circular seafloor depressions, known as pockmarks, have a
169 diameter of up to 700m, align along the crest of Vestnesa Ridge, and have a complex topography with
170 sub-depressions (pits) (Vogt et al., 1994; Bünz et al., 2012; Panieri et al., 2017b; Fig. 1c). Seepage within
171 the pockmarks Lunde and Lomvi (Fig. 1c) is heterogeneous as carbonate crusts. Findings of bacterial
172 mats and chemosynthetic tubeworms at the seafloor suggest slow and pervasive (diffuse) fluid flow
173 while flares originating from pits, smaller areas (ca. 50m in diameter) with sparse carbonate blocks at

174 the seafloor, are evidence of strong (focused) fluid flow (Panieri et al., 2017b). The pockmarks are
175 actively releasing gases into the water column in the south-eastern segment of Vestnesa Ridge but are
176 inactive in the north-western segment (Bünz et al., 2012; Smith et al., 2014; Plaza-Faverola et al., 2015).
177 Several seepage episodes since the onset of Northern Hemispheric glaciations, ca. 2.7 million (Ma)
178 years ago, and within the last 17 cal ka have been inferred from seismic interpretation of buried
179 pockmarks and mounds within chimney structures and foraminiferal stable carbon isotope records
180 (Panieri et al., 2014; Consolaro et al., 2015; Plaza-Faverola et al., 2015; Schneider et al., 2017; Sztybor
181 and Rasmussen 2017a).
182 Vestnesa Ridge is located between the western Svalbard continental margin and the ultra-slow
183 spreading Arctic ridge systems in the Fram Strait (Fig. 1a) (Talwani and Eldholm, 1977; Engen et al.,
184 2008; Johnson et al., 2015). It is bounded by the Spitsbergen Transform Fault and the ultraslow
185 spreading Molloy Ridge to the north, and the Molloy Transform Fault and the Knipovich Ridge to the
186 south (Crane et al., 2001; Vanneste et al., 2005; Winkelmann et al., 2008; Plaza-Faverola et al., 2015;
187 Johnson et al., 2015; Fig. 1a; b). Faulting and fracturing in response to tectonic stress variations over
188 the past 2.7 Ma is believed to exert an important control on seepage activity along the ridge (Plaza-
189 Faverola et al., 2015).
190 Two water masses dominate the present-day oceanographic setting of the Fram Strait: the West
191 Spitsbergen Current (WSC) and the East Greenland Current (EGC). The WSC, which is the northernmost
192 branch of the warm and saline Norwegian Atlantic Current, moves northwards along the western
193 Svalbard continental margin (Aagaard et al., 1987). It sustains ice-free conditions in the eastern Fram
194 Strait throughout most of the year and transports Atlantic water into the Arctic Ocean (Schauer et al.,
195 2004; Cokelet et al., 2008; Beszczynska-Möller et al., 2012; Rebesco et al., 2013). The EGC runs
196 southwards in the western Fram Strait and transports cold and less saline Polar Surface Water into the
197 Atlantic (Aagaard et al., 1987; Woodgate et al., 1995; Beszczynska-Möller et al., 2012).
198

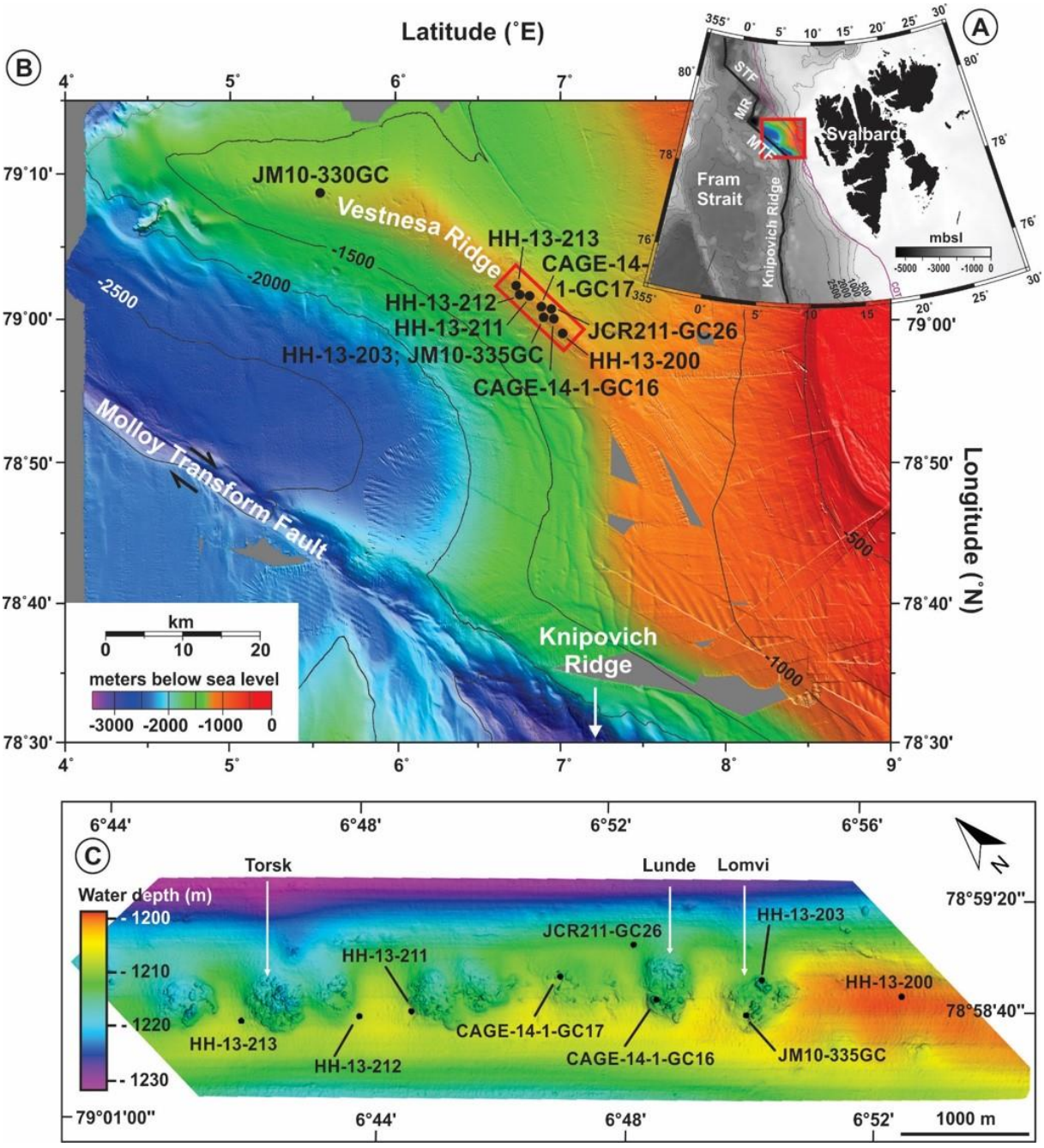

Fig. 1. (A) IBCAO map of the western Svalbard margin and eastern Fram Strait (Jakobsson et al., 2012). The red square indicates the location of inset B. The continent-ocean transition (COT) is delineated in purple. STF – Spitsbergen Transform Fault. MR – Molloy Ridge. MTF – Molloy Transform Fault. **(B)** Swath bathymetry map of Vestnesa Ridge with the location of the studied cores. The red square indicates the location of (C). Modified from Hustoft et al. (2009). **(C)** Seafloor reflection map from high resolution 3D seismic data (6x6 m bin size) showing the pockmark field on the south-eastern Vestnesa

207 Ridge segment and projection of the studied cores. Pockmark names Lunde, Lomvi and Torsk in
208 accordance with Panieri et al. (2017b).
209

210 3 Methods

211 3.1 Core collection and description

212 In this study, we examine ten sediment gravity cores collected from Vestnesa Ridge between 2008 and
213 2014 (Table 1). Eight cores were retrieved from the south-eastern segment of Vestnesa Ridge that has
214 active pockmarks (Fig. 1b). Core HH-13-200 was recovered from the southernmost location 3.5 km
215 away from the nearest active pockmark (Lomvi). In contrast, sediment core JM10-330GC was taken
216 from an inactive pockmark at the north-western ridge segment. Reference core HH-13-212 was
217 collected from a site where modern and paleo-seepage evidence was absent. The coring transect
218 covers 35.8 km with distances between the cores varying from 0.1 to 27.7 km (Table 1). Selected results
219 from these cores have already been published elsewhere (Table 1).
220 After recovery, the cores were cut into 100 cm sections, split longitudinally and kept cool at 5°C. All
221 following sediment descriptions and analyses have been performed at UiT The Arctic University of
222 Norway in Tromsø. Magnetic susceptibility (MS) and bulk density (BD) were measured in 1cm intervals
223 using a GeoTek Multi-Sensor Core Logger (MSCL). The cores were described visually, X-ray-scanned
224 (Geotek MSCL-XR 3.0), and photographed (Jai L-107CC 3 CCD RGB Line Scan Camera).
225 For reference core HH-13-212, ice-rafted debris (IRD, size > 2mm) was counted using X-ray scans.
226 Element-geochemical data from selected cores (HH-13-200; -203; -211; -213) were acquired with an
227 Avaatech XRF Core Scanner at 1 cm steps using the following settings: down-core slit size 10 mm; cross-
228 core slit size 12 mm; 10 kV; 1000 µA; no filter; and 10 seconds measuring time per step; same settings
229 but 50 kV and 20 seconds measuring time per step for barium. The raw data were subsequently
230 processed with the software WinAxil. For the purpose of this study, we show here the strontium (Sr),
231 calcium (Ca), barium (Ba), and sulphur (S) counts normalised to titanium (Ti) or normalised to the sum

of the eight most common elements in our records (Sum8) that are silicon, strontium, potassium, calcium, zirconium, rubidium, titanium, and iron.

Table 1. Coring coordinates, year of recovery, sediment recovery, depth, distance between cores, and seafloor setting of the sediment gravity cores used in this study. Cores are ordered from SE to NW.

Core ID	Coordinates	Year	Recovery (cm)	Depth (m bsf)	Distance to next core (km)	Seafloor setting	Reference and cruise
HH-13-200	78.981 °N 7.061 °E	2013	270	1205	3.70	Undisturbed seafloor	This study; Cruise CAGE-HH-2013
HH-13-203	79.002 °N 6.928 °E	2013	300	1210	0.1	Pockmark with flare (Lomvi)	Ambrose et al., 2015; Schneider et al., 2017; Cruise CAGE-HH-2013
JM10-335GC	79.002 °N 6.922 °E	2010	485	1197	0.7	Pockmark with flare (Lomvi)	Sztybor and Rasmussen 2017a; Cruise JM10
CAGE-14-1-GC16	79.008 °N 6.900 °E	2014	475	1217	0.46	Pockmark with flare (Lunde)	This study; Cruise CAGE 14-1
JCR211-GC26	79.011 °N 6.907 °E	2008	386	1210	0.60	Pockmark with flare	Panieri et al., 2014; Cruise JR211
CAGE-14-1-GC17	79.013 °N 6.880 °E	2014	440	1207	1.18	Pockmark	This study; Cruise CAGE 14-1
HH-13-211	79.018 °N 6.831 °E	2013	498	1202	0.40	Pockmark	Ambrose et al., 2015; Cruise CAGE-HH-2013
HH-13-212	*79.020 °N 6.816 °E*	*2013*	*516*	*1202*	*0.91*	*Undisturbed seafloor*	*Reference core This study; Cruise CAGE-HH-2013*
HH-13-213	79.025 °N 6.782 °E	2013	520	1203	27.76	Pockmark with flare (Torsk)	This study; Cruise CAGE-HH-2013
JM10-330GC	79.130 °N 5.600 °E	2010	420	1300		Pockmark	Consolaro et al., 2015; Cruise JM10

3.2 Chronology and age models

Stratigraphic correlation of the sediment cores is obtained through radiocarbon-dated MS records and associated tie points known from established stratigraphic marker horizons at the western Svalbard continental margin (Table 2, Jessen et al., 2010; Sztybor and Rasmussen, 2017a). All calibrated ages presented in the following text will be in calendar years before present (cal BP) A.D. 1950 with a standard deviation of 2σ.

Defined stratigraphic marker horizons include clast-rich laminated sediments (within the LGM; 24-23.5 ka), fine-grained laminated sediments (Bølling interstadial; 14.7 – 14.3 ka), and a structureless layer rich in *Coscinodiscus* spp. diatoms (Early Holocene; 10.1-9.8 ka) that have been traced along the western Svalbard continental margin between 76 and 79°N by Jessen et al. (2010; Table 2). Both the structureless diatom-rich layer and the laminated sediments require microscopic examinations of the sediment or X-ray scanning for detection. The clast-rich laminated sediment can be identified as a dark sediment layer that is characterised by a sharp drop in MS, gradually increasing BD throughout the interval, and abundant IRD (Jessen et al., 2010).

Sztybor and Rasmussen (2017a) proposed the correlation of the established stratigraphic marker horizons to the Vestnesa Ridge and provided additional radiocarbon ages. Care must be taken when using radiocarbon age determination in chemosynthetic bivalves and foraminifera from methane seeps because radiocarbon dates obtained from them often yield an older age due to exposure to methane-derived dissolved inorganic carbon and diagenetic alteration (Uchida et al., 2008). Therefore, we only use a selection of the ages obtained by Ambrose et al. (2015) and Sztybor and Rasmussen (2017a) where $\delta^{13}C$ signature is characteristic for normal marine conditions.

Table 2. Stratigraphic tie points (TP) and marker horizons from the western Svalbard continental margin used for core correlation.

Interval	Min. Age cal years BP	Max. Age cal years BP	TP	Reference
Diatom-rich layer	9,840 ± 200	10,100 ± 150	2; 3	Jansen et al., 1983; Stabell, 1986; Jessen et al., 2010; Müller and Stein, 2014
Local MS max above laminated sediment interval	14,070 ± 210		4	Jessen et al., 2010
Laminated sediment interval	14,300 ± 260	14,780 ± 220	5; 6	Elverhøi et al., 1995; Birgel and Hass, 2004; Jessen et al., 2010; Lucchi et al., 2015
Event 1	23,550 ± 185	24,080 ± 150	7; 8	Knies and Stein, 1998; Vogt et al., 2001; Jessen et al., 2010
Nearest local MS min below Event 1	27,500 ± 270		9	Jessen et al., 2010

We have further improved the stratigraphic control with one additional ^{14}C AMS radiocarbon age. The additional radiocarbon dating was carried out at the Beta Analytic Radiocarbon Dating facilities in Miami, US. A conventional radiocarbon age of 28,090 +/- 150 years was obtained from a basal sample of core HH-13-213 (455 cm, laboratory code Beta-456619). The age was converted into calendar years using the calibration program Calib 7.1 (Stuiver et al., 2014) with a marine reservoir age of -400 years that was incorporated within the Marine13 calibration curve (Reimer et al., 2013). In addition, a regional reservoir age correction ΔR of 7 ± 11 was applied (Mangerud et al., 2006). The age model is based on the calibrated ages obtained from the peaks of the probability curves within the 2σ range. The calibrated result was an age of 29,490 +/- 287 years BP. Based on the stratigraphic tie points (Table 2) and the additional radiocarbon age, we calculate linear sedimentation rates for the stratigraphic marker horizons and the intermediate sediment intervals (supplementary material S1).

3.3 Stable isotope analyses of foraminifera

Samples for stable isotope analysis of foraminiferal calcite tests were typically collected at 10 cm intervals and at 5 cm intervals from the reference core HH-13-212 (Table S2). Samples from cores HH-

13-203 (depth interval from 220 to 270 cm) and HH-13-211 (depth interval from 390 to 470 cm) were obtained at higher spatial resolution (Table S2). The samples were wet-weighed, freeze-dried, dry-weighted, and wet-sieved (mesh sizes 63µm, 100µm, 1mm). The sieve residues were dried at 40°C and subsequently investigated using light microscopes. Benthonic (*Cassidulina neoteretis* [Seidenkrantz, 1995]; *Melonis barleeanus* [Williamson, 1858]) and planktonic foraminifera (*Neogloboquadrina pachyderm*a sin [Ehrenberg, 1861]) were picked for isotope measurements from the dry residue of the >100 µm size fraction. Those species were selected since they are abundant throughout the cores, and common in the Arctic Ocean (Wollenburg and Mackensen 1998; Wollenburg et al., 2001; Zamelczyk et al., 2012). The same foraminiferal species have been used in similar studies from Vestnesa Ridge (Table 1).

Stable oxygen ($\delta^{18}O$) and carbon ($\delta^{13}C$) isotope analyses of foraminiferal tests were performed using a ThermoFinnigan MAT252 mass spectrometer coupled to a CarboKiel-II carbonate preparation device at the Serveis Cientifico-Técnics of the University in Barcelona in Spain. *Cassidulina neoteretis (236 samples)*, *M. barleeanus (18 samples), N. pachyderm*a sin (172 samples) were picked for isotope analyses. Each sample consists of 15 to 30 tests. Analytical precision was estimated to be better than ±0.08‰ for oxygen and ±0.03‰ for carbon by measuring the certified standard NBS-19. We report all isotope results in standard delta notation relative to Vienna Pee Dee Belemnite (VPDB). For already published stable isotope records that are included in this study, details for sample preparation and stable isotope measurements can be found in the references given in Table 1.

3.4 MDAC analyses – stable isotopes and mineralogy

Stable oxygen ($\delta^{18}O$) and carbon ($\delta^{13}C$) isotope analyses of 37 authigenic carbonate nodules from different cores were performed using a ThermoScientific MAT253 mass spectrometer coupled to a Finnigan Gasbench II at the Stable Isotope Laboratory at UiT The Arctic University of Norway in Tromsø. Analytical precision was estimated to be better than ±0.07‰ VPDB.

Where enough material was present, we performed XRD analyses of unoriented carbonate samples using a Bruker D8 Advance X-ray diffractometer (Cu K_α radiation in 3-75° 2θ range) at the Geological Survey of Norway, Trondheim. The quantitative mineralogical composition of the carbonate phases was interpreted and modelled by using the Rietveld algorithm-based code Topas-4 by Bruker. Following a displacement correction of the spectrum made on the main quartz peak, the displacement of calcite d_{104} was used to estimate the amount of $MgCO_3$ mol % (Goldsmith and Graf, 1958).

4 Results and Discussion

4.1 Lithology, chronology and core correlation

The length of the ten investigated sediment cores varies between 2.7 and 5.2 m with an approximate age range from 31.9 ka BP (Late Glacial) to 10 ka BP (Early Holocene). The sedimentological description and the chronological framework of already published cores can be found in the references given in Table 1.

4.1.1 Reference core HH-13-212 and regional correlations

The 519 cm long reference core HH-13-212 was collected outside pockmarks on the crest of Vestnesa Ridge where methane seepage is absent. The core is composed of silty clay with intervals rich in IRD and includes all three main stratigraphic marker horizons for the western Svalbard continental margin spanning from the LGM to the Early Holocene (Tab. 3; Fig. 2). The diatom-rich interval occurs in the top 5 cm of the core (max. age 10.1 ka BP; Early Holocene), laminated sediments occur between 65 cm (14.3 ka BP) and 155 cm (14.7 ka BP; Bølling), and dark laminated coarser sediment occurs at 309-353 cm (24-23.5 ka BP; within the LGM; Tab. 3; Fig. 2). This interval known as “Event 1” (Knies and Stein, 1998) is dated to approximately 23-19.4 ^{14}C ka BP (Elverhoi, 1995; Andersen et al., 1996; Vogt et al., 2001) or 24 ka BP (^{14}C age: 20,040 $\pm$ 325; lab code KIA365, Knies and Stein, 1998).

The MS values largely follow the western Svalbard MS stack curve (Jessen et al., 2010, Fig. 2). For the description of the lithology and foraminifera content of core HH-13-212, the main stratigraphic marker

horizons, and major paleoceanographic and environmental changes the reader is referred to supplementary material S2.

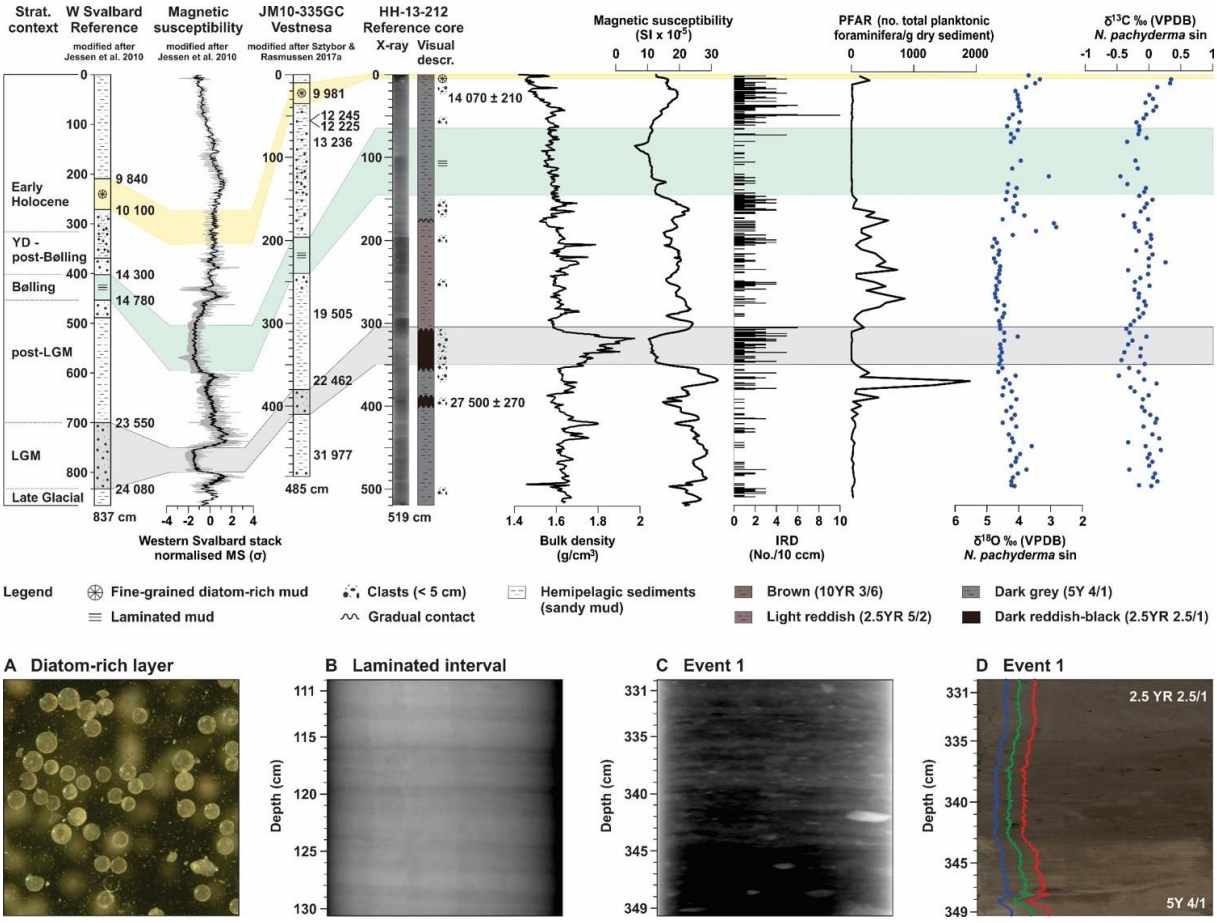

Fig. 2. Lithology and magnetic susceptibility (MS) of the western Svalbard reference record obtained by Jessen et al. (2010). Lithology of core JM10-335GC modified after Sztybor and Rasmussen (2017a). X-ray image, lithology, BD, MS, IRD content, PFAR (planktonic foraminiferal accumulation rate), stable oxygen and carbon isotope records from *N. pachyderma* sin from Vestnesa Ridge reference core HH-13-212. LGM – Last Glacial Maximum. HE 1 – Heinrich Event 1. YD – Younger Dryas. The negative MS peaks at 100 and 500 cm are artefacts due to change in core section. **(A)** Diatom-rich interval. Photograph of the > 63µm fraction from microscope, magnification is 16x. HH-13-212, 5cm bsf. **(B)** Laminated interval. X-ray scan of fine-grained laminated sediments. HH-13-212, 110-131cm bsf. **(C)** Event 1 sediments. X-ray scan of fine-grained laminated sediment providing a matrix for abundant

gravel sized clasts. HH-13-212, 330-350 bsf. **(D)** Event 1 sediments. Colour scan, RGB colour values, and lower contact of the Event 1 interval. HH-13-212, 330-350cm bsf.

4.1.2 Cores from active and inactive pockmarks on Vestnesa Ridge

The eight sediment cores recovered from active or inactive pockmarks, and the southernmost core HH-13-200, consist of dark grey silty clay of late Pleistocene and Early Holocene age with layers rich in IRD, and shell fragments (Fig. 3).

Magnetic susceptibility signals are typically low (Table 4). This is common in methane seeps where iron-oxides such as ferromagnetic magnetite (Fe_3O_4) are exposed to hydrogen-sulphide produced by AOM, experience reduction to paramagnetic pyrite (FeS_2), and cause significant reduction or loss of the MS signal (Canfield and Berner, 1987; Riedinger et al., 2005; März et al., 2008; Dewangan et al., 2013). Nevertheless, all three typical stratigraphic marker horizons can be recognised in most of the sediment cores and allow core correlation (Table 3). The 25-50cm thick Event 1 sediments were identified based on X-ray images and a reddish-black layer (Munsell colour: 2.5YR 2.5/1) in cores CAGE-14-1-GC16; CAGE-14-1-GC17; HH-13-211, and HH-13-213. A radiocarbon date of 24,743 years BP at 460.5 cm obtained from planktonic foraminifera confirms the upper boundary of Event 1 (Ambrose et al., 2015). The total thickness of the laminated interval varies between 30cm and 90cm. In most cores, the interval rich in *Coscinodiscus* spp. diatoms occurs at or near the core top, indicating Early Holocene-aged sediments near the seafloor. The calculated linear sedimentation rates reveal rapid sedimentation during LGM (75-90 cm kyr^{-1}) and the Early Holocene (67-188 cm kyr^{-1}; supplementary material S1).

Interestingly, sediment cores from the western Svalbard continental shelf and slope, including south-eastern Vestnesa Ridge segment, share the absence of Early Holocene sediments (Elverhøi et al., 1995; Howe et al., 2008; Sztybor and Rasmussen 2017a; 2017b). At a water depth of 1200m, the south-eastern segment of Vestnesa Ridge may be exposed to the erosive force of the WSC resulting in non-deposition or sediment removal. Mooring studies across the Fram Strait reveal the present-day WSC

375 has two branches with a narrow and strong core shallower than 1000m and maximum northwards
376 velocities of 20 cm s^{-1}, and an offshore branch below 1400m with northwards velocities of 5-10 cm s^{-1}
377 (Beszczynska-Möller et al., 2012; Rebesco et al. 2013). The strong WSC core may have winnowed
378 unconsolidated fine-grained sediments from the easternmost part of Vestnesa Ridge, explaining the
379 narrow and sharp bathymetric expression of the ridge along its eastern segment compare to the west
380 (Fig. 1). In contrast, the north-western ridge segment, located in 1300m water depth, has a more
381 widespread and gently rounded geometry. It may have experienced less strong current velocities and
382 therefore retained Holocene sediments.
383

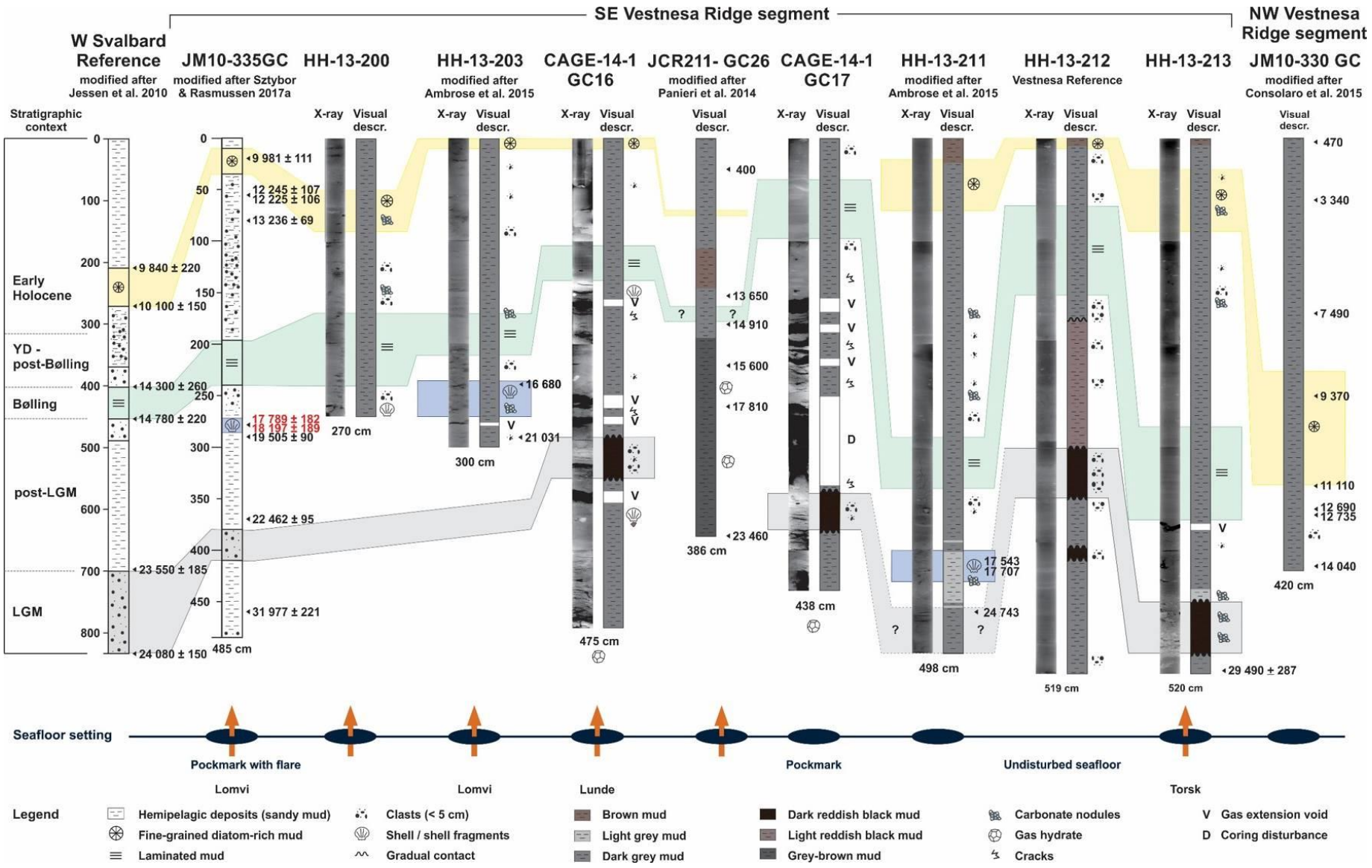
SE Vestnesa Ridge segment
NW Vestnesa Ridge segment
W Svalbard Reference
modified after Jessen et al. 2010
JM10-335GC
modified after Sztybor & Rasmussen 2017a
HH-13-200
HH-13-203
modified after Ambrose et al. 2015
CAGE-14-1 GC16
JCR211- GC26
modified after Panieri et al. 2014
CAGE-14-1 GC17
HH-13-211
modified after Ambrose et al. 2015
HH-13-212
Vestnesa Reference
HH-13-213
JM10-330 GC
modified after Consolaro et al. 2015
Stratigraphic context
X-ray
Visual descr.
Early Holocene
YD - post-Bølling
Bølling
post-LGM
LGM
9 981 ± 111
12 245 ± 107
12 225 ± 106
13 236 ± 69
9 840 ± 220
10 100 ± 150
14 300 ± 260
14 780 ± 220
17 789 ± 182
18 197 ± 185
19 505 ± 90
22 462 ± 95
23 550 ± 185
31 977 ± 221
24 080 ± 150
485 cm
270 cm
300 cm
16 680
21 031
475 cm
400
13 650
14 910
15 600
17 810
23 460
386 cm
438 cm
17 543
17 707
24 743
498 cm
519 cm
520 cm
29 490 ± 287
470
3 340
7 490
9 370
11 110
12 690
12 735
14 040
420 cm
Seafloor setting
Pockmark with flare
Pockmark
Undisturbed seafloor
Lomvi
Lomvi
Lunde
Torsk
Legend
Hemipelagic deposits (sandy mud)
Fine-grained diatom-rich mud
Laminated mud
Clasts (< 5 cm)
Shell / shell fragments
Gradual contact
Brown mud
Light grey mud
Dark grey mud
Dark reddish black mud
Light reddish black mud
Grey-brown mud
Carbonate nodules
Gas hydrate
Cracks
V Gas extension void
D Coring disturbance

385

386 **Fig. 3.** Core description and correlation with published records from Vestnesa Ridge and the western
387 Svalbard margin. Note the different depth scale on the W Svalbard reference record. The depth of the
388 laminated sediments in core JCR211-GC26 was estimated assuming linear sedimentation between the
389 ages obtained by Panieri et al. (2014). Ages given in red yield a too old date. Pockmark names according
390 to Panieri et al. (2017b). LGM – Last Glacial Maximum. HE 1 – Heinrich Event 1. YD – Younger Dryas.

391

392

393 **Table 3.** Depth intervals of the main sedimentary units and fossil content, given in cm below seafloor
394 (bsf). *The depth of the laminated sediments in core JCR211-GC26 was estimated assuming linear
395 sedimentation between the ages obtained by Panieri et al. (2014). bsf - below sea floor.

396

Core ID	**Diatom-rich sediments** cm bsf	**Laminated sediments** cm bsf	**Shell bed** cm bsf	**Event 1** cm bsf
HH-13-200	50-90	170-240	-	-
HH-13-203	0-10	172-210	236-268	-
JM10-335GC	10-35	200-240	278	380-410
CAGE-14-1-GC16	0-10	105-137	-	290-330
JCR211-GC26	117-120	167-178*	-	-
CAGE-14-1-GC17	-	40-98	-	347-372
HH-13-211	20-70	287-340	400-430	? (> 465)
HH-13-212	0-5	65-155	-	309-353
HH-13-213	30-90	280-370	-	450-498
JM10-330 GC	225-335	-	-	-
Time Period	**Early Holocene**	**Bølling interstadial**	**HE 1**	**LGM**
Age (cal years BP)	10,080-9,840	14,780-14,300	17,707-16,680	23,550-24,080

Interpretation	Northward movement of the Oceanographic Polar Front	Deglacial plumite from rapid SBIS disintegration	Seafloor methane seepage	SBIS maximum extent during LGM
Reference	Jansen et al., 1983; Stabell, 1986; Jessen et al., 2010; Müller and Stein, 2014	Elverhøi et al., 1995; Birgel and Hass, 2004; Jessen et al., 2010; Lucchi et al., 2015	Bond et al., 1992; Hemming, 2004; Ambrose et al., 2016; Stzybor and Rasmussen, 2017a	Knies and Stein, 1998; Vogt et al., 2001; Jessen et al., 2010

In the recovered sediments, the following features were caused by the presence of methane and microbially mediated AOM. Firstly, the cores retrieved from pockmarks with active flares had a strong odour of hydrogen-sulphide (H_2S). Secondly, the present-day SMTZ is shallow in cores HH-13-200; -203 and JCR211-GC26, as revealed by porewater data (Hong et al., 2016, Table 4). The present-day SMTZs are located at 100-140cm bsf in HH-13-203 and at 70-120cm bsf in JCR211-GC26, which have estimated depositional ages of 13.4 ka and 4.8 ka, respectively (Table 4). Thirdly, near-surface gas hydrate was recovered in cores CAGE-14-1-GC16 (in core catcher), CAGE-14-1-GC17 (in core catcher), and JCR211-GC26 (hydrate bearing sediment at 200-380cm, Fig. 3). Fourthly, irregularities such as cm-scale voids and cracks in cores where gas hydrate was recovered are likely to be introduced by gas expansion during core recovery, while the dm-scale void in CAGE-14-1-GC17 may result from coring disturbance. Finally, carbonate nodules occur in cores HH-13-203 (220-280cm), HH-13-211 (470-498cm), and in core HH-13-213 below 450cm bsf (Fig. 3). Additional mm-sized micritic carbonates were found throughout the cores named above, and in HH-13-200 when examining the >100µm coarse fraction for foraminiferal studies.

Table 4. Depth of the SMTZ in the studied cores, host sediment age, and description of magnetic susceptibility data (MS). Host-sediment age at the SMTZ position was calculated from linear sedimentation rates (S1). *Hong et al. 2016. ** Ambrose et al. 2015.

Core ID	**Present-day SMTZ** (cm bsf)	**Host sediment age at SMTZ position** (cal ka BP)	**MS**
HH-13-200	75-115*	11.4 – 10	Depleted
HH-13-203	100-140*	13.4 – 12.4	Depleted**
JM10-335GC	–	–	Depleted
CAGE-14-1-GC-16	–	–	Depleted
JCR211-GC26	70-120*	10.1 – 4.8	no data
CAGE-14-1-GC-17	–	–	Depleted
HH-13-211	165-225	13.1 – 11.9	Depleted**
HH-13-212	–	–	Normal
HH-13-213	70-100	10.3 – 10	Depleted
JM10-330 GC	–	–	Normal
Time frame (cal years BP)	recent	13.4 – 4.8	
Interpretation	SO_4^{2-}-CH_4 interface, occurrence of SO_4^{2-}-dependent AOM	SMTZ in ancient host sediments	AOM-related exposure to H_2S

Complete valves and shell fragments of juvenile and mature bivalves and gastropods in cores HH-13-203 and HH-13-211 (Fig. 3) represent a chemosynthetic bivalve community (hereafter named "shell bed") that was described for the first time in Ambrose et al. (2015). *Vesicomydae* bivalves dominate the species assemblage (Hansen et al., 2017). Some bivalves and ostracods were found with articulated valves, indicating they likely died *in-situ*. Ambrose et al. (2015) dated the shell bed to 16,680 to 17,707 cal years BP using planktonic foraminifera and bivalves without MDAC overgrowth and $\delta^{13}C$ values

higher than -1.6‰ that suggest valid ages.

4.2 Stable isotope records

4.2.1 Stable oxygen isotopes

Our records are consistent with the $\delta^{18}O$ stratigraphy for planktonic foraminifera from the western Svalbard margin (e.g. Elverhøi et al., 1995; Nørgaard-Pedersen et al., 2003; Rasmussen et al., 2007), the Yermak Plateau (Nørgaard-Pedersen et al., 2003) and the northern Barents Sea margin (Knies et al., 1999; 2000) during the LGM, post-LGM and Early Holocene.

$\delta^{18}O$ values from planktonic foraminifera during the LGM in the Fram Strait are typically around 4.5 to 4.8‰ (e.g. Hebbeln et al., 1994; Elverhøi et al., 1995; Nørgaard-Pedersen et al., 2003). We obtain similar values during the LGM (Figs. 2a and 4a; CAGE-14-1-GC16; HH-13-212). Termination 1 (17.8-16.7 ka BP) is defined by low $\delta^{18}O$ values indicative of melt-water contributions from the SBIS and can be recognised in the entire Polar North Atlantic (Hebbeln et al., 1994; Elverhøi et al., 1995; Nørgaard-Pedersen et al., 2003).

At Vestnesa Ridge, two spikes of values as low as 2.8-3‰ in *N. pachyderma* sin occur in post-LGM and Bølling interstadial-aged sediments (Figs. 2a and 4a, HH-13-212; CAGE-14-1-GC16). We suggest the first $\delta^{18}O$ spike in the post-LGM sediments marks Termination 1, and the second $\delta^{18}O$ spike indicates iceberg calving and meltwater discharge during the Bølling-Allerød interstadials. During the Early Holocene, $\delta^{18}O$ values generally decrease. An additional, less pronounced $\delta^{18}O$ spike in the Younger Dryas (Figs. 2a and 4a; HH-13-212; CAGE-14-1-GC16), signals the beginning of interglacial conditions when northwards protruding warm Atlantic water masses destabilised the ice tongues of tidewater glaciers and may have caused local meltwater pulses in the northern North Atlantic (Elverhøi et al., 1995; Rasmussen et al., 2007; Slubowska-Woldengen et al. 2007; Consolaro et al., 2015; Consolaro et al. accepted manuscript).

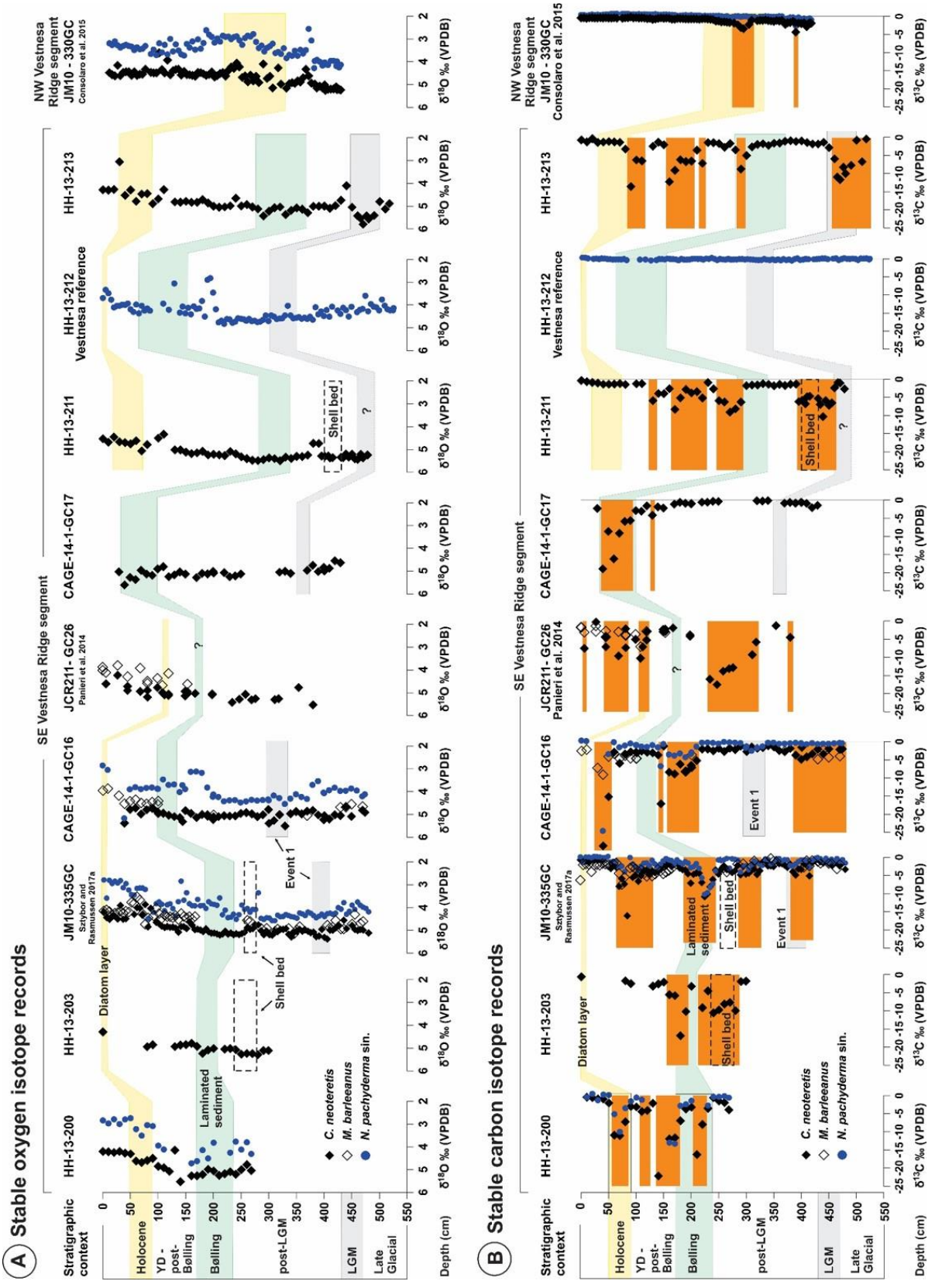

Fig. 4. $\delta^{18}O$ **(A)** and $\delta^{13}C$ **(B)** records (*C. neoteretis; M. barleeanus*) and planktonic (*N. pachyderma* sin) foraminifera. The Early Holocene diatom layer (9.8-10.1 ka BP), the laminated sediment deposited

during the Bølling interstadial (14.3-14.8 ka BP), and near the LGM (23.5-24 ka BP) are indicated. LGM – Last Glacial Maximum. HE 1 – Heinrich Event 1. YD – Younger Dryas. Orange zones are indicating the events of negative carbon excursions. See supplementary material S3 for the foraminiferal stable carbon and oxygen isotope values.

4.2.2 Stable carbon isotopes

The $\delta^{13}C$ record of planktonic *N. pachyderma* sin from core HH-13-212 (Figs. 2; 4b) ranges between 0 and -1‰ and can be considered as representative for normal marine conditions, expressed as $\delta^{13}C$ values between -0,5 and 0.5‰ (Knies and Stein, 1998). A $\delta^{13}C$ range between 0 and -1‰ is considered representative for normal marine conditions in benthonic *C. neoteretis* tests from the northern Barents Sea (0 to -1‰, Wollenburg et al., 2001) and a control site from the Håkon Mosby Mud Volcano (-1.15‰, Mackensen et al., 2006). For *M. barleeanus,* McCorkle et al. (1990) observed $\delta^{13}C$ values of -2‰ in the Atlantic Ocean.

In contrast, the majority of the $\delta^{13}C$ r of benthonic and planktonic foraminifera show between two and five negative $\delta^{13}C$ excursions with amplitudes up to -29‰, separated by one or more intervals containing foraminifera with $\delta^{13}C$ values typical for normal marine conditions (Fig. 4b). Negative $\delta^{13}C$ excursions in benthonic foraminifera occur in LGM sediments (HH-13-211; -213; JM10-335GC), during HE 1 (HH-13-203; -211), during and after the Bølling interstadial (HH-13-200; -203; JM10-335GC; CAGE-14-1-GC16; CAGE-14-1-GC17; HH-13-211; -213), and during the Early Holocene (HH-13-200; JCR211-GC26). In some intervals, negative $\delta^{13}C$ excursions co-occur in benthonic and planktonic foraminifera (HH-13-200, 60,5-220,5 cm; CAGE-14-1-GC16, 144,5-209,5 cm), while in others exclusively benthonic foraminifera are ^{13}C depleted (CAGE-14-1-GC16, 359,5-439,5 cm; JM10-330GC, 255-305 cm).

Living foraminifera can incorporate ^{13}C-depleted, methane-derived dissolved inorganic carbon (DIC) while metabolically active, and/or likely ingestion of ^{13}C-depleted methanotrophic microbes, leading to slightly negative $\delta^{13}C$ values as low as -5.6‰ (Rathburn et al., 2003; Hill et al., 2004; Panieri et al., 2006; Panieri and Sen Gupta, 2008). However, values as low as -15‰, as we record in planktonic

foraminifera, and -29‰ in benthonic foraminifera, cannot be explained solely by metabolic activity of the foraminifera in the presence of methane-derived DIC or foraminiferal diet. Furthermore, planktonic foraminifera living in the surface water are unlikely to encounter AOM-derived DIC as benthonic organisms consume most of the methane (Damm et al., 2005; Niemann et al., 2006; Reeburgh, 2007; Boetius and Wenzhöfer, 2013; Steinle et al., 2015). The strong negative $\delta^{13}C$ signatures are most likely introduced after the death of the foraminifera and burial of their tests in the sediment through the diagenetic alteration at the SMTZ. Panieri et al. (2017a) investigated the boundaries between biogenic test calcite and diagenetic overgrowth and showed that foraminiferal tests act as nucleation templates for MDAC. Schneider et al. (2017) described the visual and geochemical characteristics of foraminiferal tests experiencing diagenetic alteration during methane seepage. Such MDAC precipitation at the SMTZ cumulatively adds a second phase of ^{13}C-depleted carbon on foraminiferal tests and causes negative $\delta^{13}C$ values in the range of -7 to -36‰ (Torres et al., 2003b; Hill et al., 2004; Millo et al., 2005; Panieri et al., 2009; Martin et al., 2010; Panieri et al., 2017a; Sztybor and Rasmussen, 2017a; 2017b; Schneider et al., 2017). We follow this interpretation and suggest that each negative $\delta^{13}C$ excursion is caused by diagenetic alterations of the primary tests and indicates a relatively stable SMTZ at/close to the seafloor due to enhanced methane flux.

Exclusively in the reference core HH-13-212, which is located close to active pockmarks, evidence for methane seepage and MDAC precipitation are entirely absent in planktonic foraminiferal $\delta^{13}C$ records. Cores from pockmarks at the south-eastern ridge segment have the largest variability and amplitudes in $\delta^{13}C$ while the north-western most core, JM10-330 GC, only shows two negative $\delta^{13}C$ excursions of comparably small amplitude (Fig. 4b). The easternmost core, HH-13-200, surprisingly shows negative $\delta^{13}C$ excursions although the core has been recovered in 3.5 km distance to the nearest active pockmark (Lomvi). This may be the case explained by the proximity of the core-site to non-outcropping fluid flow related features, as observed in seismic data (unpublished data).

4.3 Dynamic SMTZ migration in ancient sediments

Negative foraminiferal $\delta^{13}C$ excursions are typically associated with elevated sediment Ca/Ti and Sr/Ti elemental ratios and with the presence of carbonate-cemented nodules in cores HH-13-200; -203; -211; and -213 (Figs. 5; 6). Elevated Ca/Ti elemental ratios identify sediment intervals with high Ca-carbonate content, which can have biogenic origin, such as abundant foraminiferal tests or calcite shells of larger animals, or inorganic origin due to MDAC precipitates. Peaks in Ca/Ti near the base of cores HH-13-203 (Fig. 5b) and HH-13-211 (Fig. 6a) are caused by bivalves and gastropods of the shell bed as described by Ambrose et al. (2015). Large carbonate clasts in core HH-13-213 prevented XRF measurements deeper than 450 cm (Fig. 6b), but an initial rise in Sr and Ca content indicate elevated carbonate content towards the base of the core. Elevated Sr values are typical for aragonite, a common constituent of MDAC (Kastner et al., 1990) that precipitates when the SMTZ is close to the sediment-water interface. The $\delta^{13}C$ values of the carbonate nodules range between -36.58‰ and -8.59‰ (supplementary material S4). Our XRD analyses (supplementary material S5) indicate that high-Mg calcite (5-20mol% $MgCO_3$, Burton 1993) dominates the carbonate phase in the nodules from HH-13-203 (Fig. 5b). High-Mg-calcite and aragonite comprise the carbonate phase in the nodules from HH-13-213 (Fig. 6b). In HH-13-211 additional small fractions of low-Mg calcite (<5mol% $MgCO_3$, Burton 1993) and Mg-poor dolomite are present (Fig. 6a). An earlier study of the shell bed host sediments in core HH-13-203 reveals the presence of pyrite-encrusted tube-like features, framboidal pyrite, and botryoidal aggregates of acicular aragonite crystals (Ambrose et al., 2015), and the carbonate nodules composed of irregularly shaped 5-10µm sized carbonate crystals with disseminated pyrite that are cementing detrital grains (Schneider et al., 2017). The carbonate isotope signatures, their mineral composition, and co-occurring chemosynthetic bivalves suggest the carbonates are methane-derived and formed when the SMTZ was located at the seafloor (Aloisi et al., 2000; Bohrmann et al., 2001; Greinert et al., 2001; Naehr et al., 2007; Ambrose et al., 2015). We hence regard sediment records of MDACs, negative foraminiferal $\delta^{13}C$ excursions and elevated Ca/Ti and Sr/Ti elemental ratios as

indicators of multiple (past) SMTZ positions and subseafloor diagenetic methane cycling (grey bars in Figs. 5; 6).

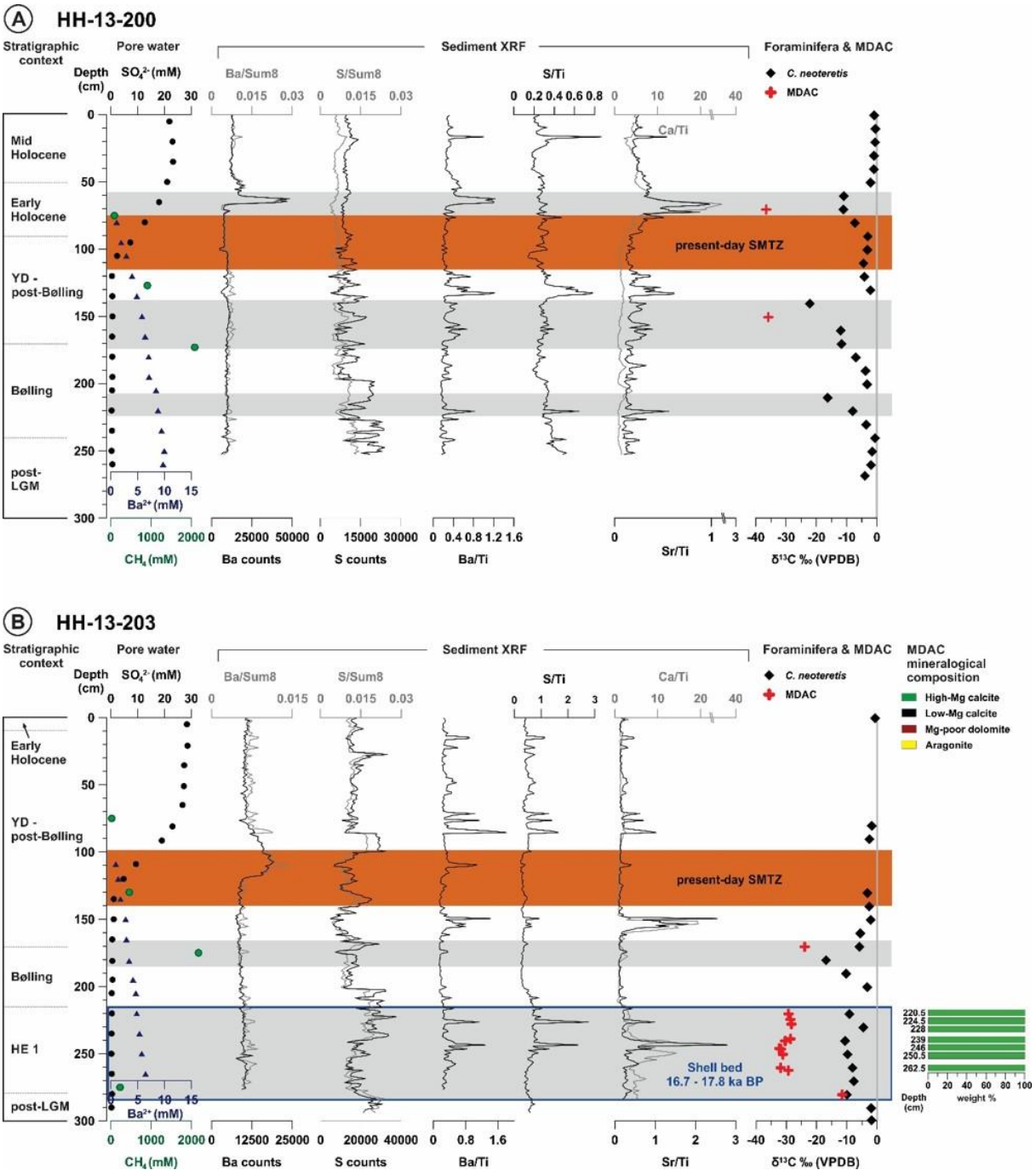

Fig. 5. Porewater data according to Hong et al. (2016), sediment elemental ratios, $\delta^{13}C$ of benthonic foraminifera (*C. neoteretis*), and mineralogical composition of the MDAC nodules of **(A)** HH-13-200 and

(B) HH-13-203. The orange box indicates the present-day SMTZ as derived from porewater data. Grey bars indicate negative foraminiferal $\delta^{13}C$ excursions. Position of the shell bed in HH-13-203 according to Ambrose et al. (2015) (blue box). YD – Younger Dryas. HE 1 – Heinrich Event 1. Ba – Barium. S – Sulphur. Ti – Titanium. Ca – Calcium. Sr – Strontium. Sum8 - sum of the eight most common elements in our record. Note varying scales.

A common approach to determine the present-day SMTZ position is using the mutual depletion of sulphate and methane concentrations in porewater (e.g. Jørgensen and Kasten, 2006). The present-day SMTZ in core HH-13-200 is at 75-115cm (Tab. 4, Hong et al., 2016; host sediment age ca. 11.4-10 ka, Early Holocene, Fig. 5a), and in core HH-13-203 at 100-140cm (Tab. 4, Hong et al., 2016; host sediment age ca. 13.4-12.4 ka, Allerød interstadial/Younger Dryas, Fig. 5b). From modelling of sulphate reduction rates, Hong et al. (2016) suggest the SMTZ has been stable for 50 (HH-13-203) to 100 years (HH-13-200). Assuming persistent diffuse seepage where the SMTZ remained long enough at the same position, detectable carbonate precipitation in the sediments and on microfossils is likely to occur. In cores where porewater data are absent (HH-13-211 and HH-13-213), we use barium and sulphur elemental ratios to identify the tentative SMTZ position (Fig. 6). Our approach is based on sediment and porewater Ba profiles that depend on sulphate availability as initially described by Torres et al. (1996). According to previous studies (Torres et al., 1996; Dickens, 2001; Sauer et al. 2017), Ba/Ti peaks immediately above increasing S/Ti concentrations are indicative of the SMTZ position, while double Ba-peaks indicate recent vertical movement of the SMTZ (Riedinger et al., 2005). In sediment XRF records of core HH-13-200 a sharp peak in Ba and Ba/Ti occurs directly above the present-day SMTZ (Fig. 5a), suggesting the precipitation of diagenetic barite. In HH-13-203, multiple Ba/Ti peaks occur above the present-day SMTZ (Fig. 5b). Sulphur counts in the sediment of both cores are low within and above the SMTZ but increase underneath (Fig. 5), interpreted to reflect increasing amounts of authigenic pyrite (Neretin et al., 2004; Jørgensen and Kasten, 2006).

Sediment XRF ratios for Ba/Ti and S/Ti along with foraminifera and MDAC records from cores HH-13-

583 211 and HH-13-213 are presented in Figure 6. In HH-13-211, a paprominent Ba/Ti peak is located
584 immediately above a steep rise in S/Ti (Fig. 6a; 165-225cm). In HH-13-213, the level with multiple Ba/Ti
585 peaks is located directly above a zone with rising S/Ti at the depth of 70-100cm (Fig. 6b). Indicated by
586 the largest barium peak and further geological evidence such as MDAC nodules, negative foraminiferal
587 $\delta^{13}C$ excursions and elevated Sr/Ti ratios at corresponding depth (Fig. 6), the tentative present-day
588 SMTZ in core HH-13-211 is at 165-185cm (host sediment age ca. 11.9-12.3 ka, Younger Dryas, Fig. 6a)
589 while it is at 70-100cm in core HH-13-213 (host sediment age ca. 10.3-10 ka, Early Holocene, Fig. 6b).
590

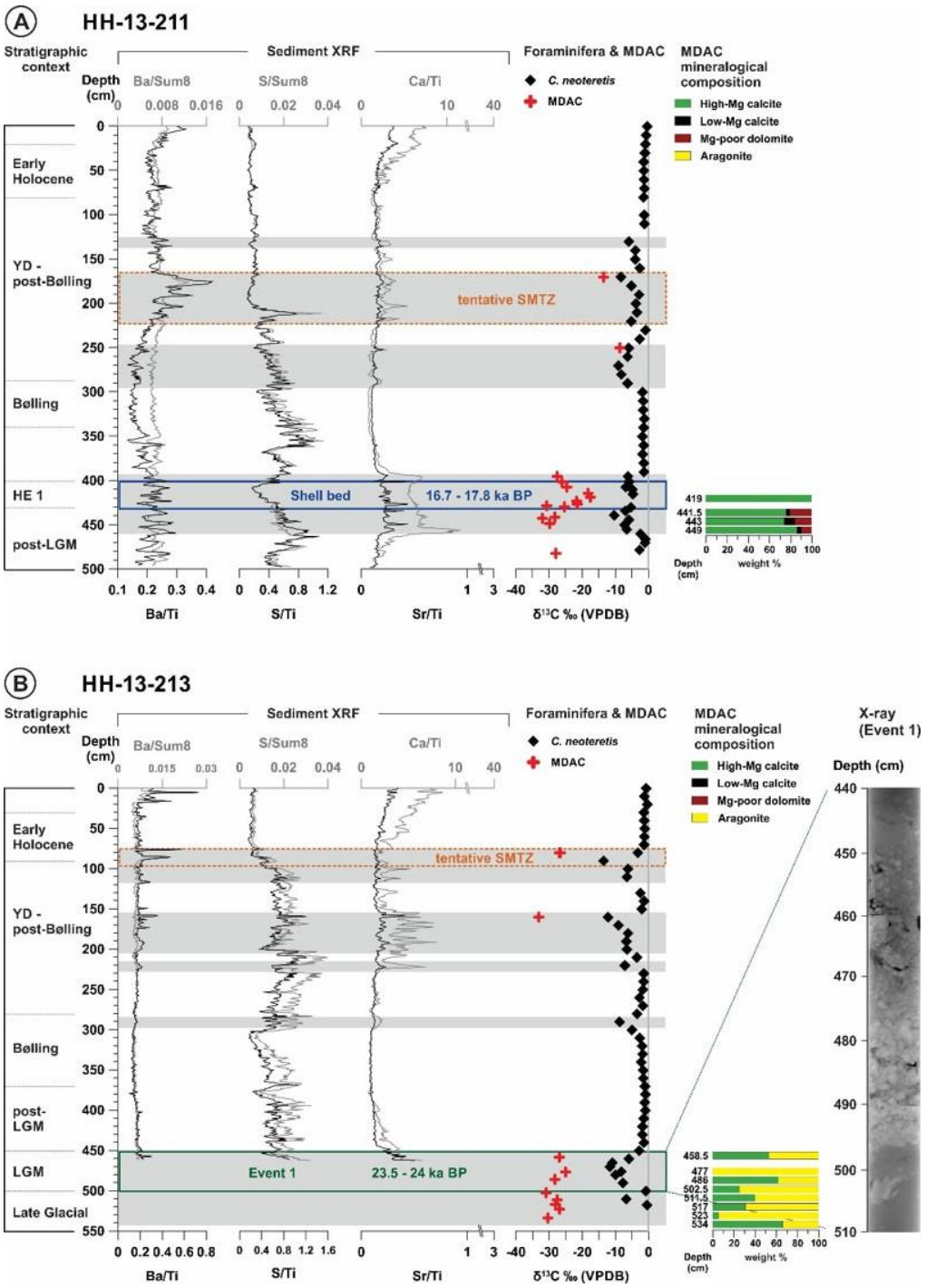

Fig. 6. Sediment elemental ratios, $\delta^{13}C$ of benthonic foraminifera (*C. neoteretis*) and mineralogical composition of the MDAC nodules of **(A)** HH-13-211 and **(B)** HH-13-213. The dashed orange box indicates the tentative SMTZ. Position of the shell bed in HH-13-211 according to Ambrose et al. (2015) (blue box). Grey bars indicate negative foraminiferal $\delta^{13}C$ excursions. YD – Younger Dryas. HE 1 – Heinrich Event 1. Ba – Barium. S – Sulphur. Ti – Titanium. Ca – Calcium. Sr – Strontium. Sum8 - sum of the eight most common elements in our record. Note varying scales.

4.4 Timing of past seepage events at Vestnesa Ridge

Along the Vestnesa Ridge transect, 32 sediment intervals tracking subseafloor methane cycling and/or seepage events occur in studied cores (Fig. 4). We observe one major event that coincides with the LGM (24-23.5 ka BP), additional events coinciding with the HE 1 (17.7-16.7 ka BP), and multiple isolated events in up to 13.4 ka old host sediment (Fig. 7).

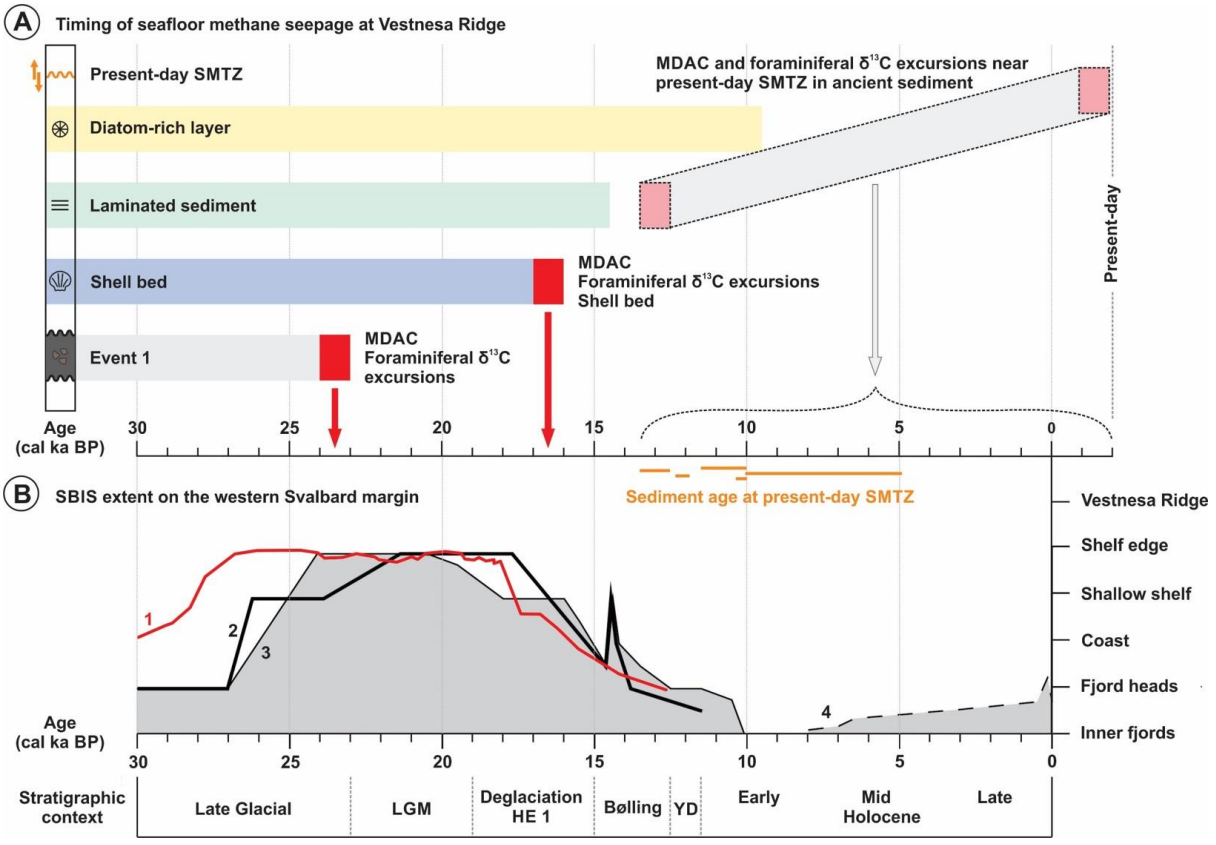

Fig. 7. (A) Timing of methane seepage at Vestnesa Ridge. MDAC nodules, negative $\delta^{13}C$ excursions in foraminiferal records, and the shell bed document main methane seepage episodes at Vestnesa Ridge in sediments deposited at the LGM, during HE 1, and isolated episodes due to diagenetic methane cycling at vertically migrating SMTZs in younger sediments. **(B)** SBIS extent at western Svalbard during the past 30 ka. LGM – Last Glacial Maximum. HE 1 – Heinrich Event 1. YD – Younger Dryas. Modified from Jessen et al. (2010). SBIS ice extend curves are based on (1): Patton et al. (2015),

(2): Elverhøi et al. (1995), (3): Jessen et al. (2010), (4): Svendsen and Mangerud (1997).

Assessing the timing of past methane seepage is challenging since the ages that MDAC that carry form in a diagenetic realm and are independent from the host sediment age. The precipitation age of aragonite-rich MDAC, which are free of detrital impurities, can be determined using U/Th chronology (Teichert et al., 2003; Bayon et al., 2009; 2013; Crémière et al., 2016b; Sauer et al., 2017). Here, available MDAC nodules are not suitable for U/Th geochronology, and therefore, only their occurrences below the present-day SMTZ can indirectly constrain the timing of subseafloor methane enrichment and methane seepage.

Abundant MDAC nodules at the base of core HH-13-213 are restricted to the Event 1 sediments (ca. 24-23.5 ka BP; Fig. 6) with high sedimentation rates (S2). We suggest the carbonate precipitation in these LGM sediments occurred syn-sedimentary or shortly post-dating the deposition, consistent with the aragonite dominance of the MDAC nodules implying high methane flux and the SMTZ position very close to the seafloor. Thus, the oldest event of subseafloor methane enrichment in this dataset corresponds to the SBIS LGM shelf edge glaciation at ca. 24 ka BP (Fig. 7; Hormes et al., 2013; Patton et al., 2015 and references therein).

The shell bed (Ambrose et al., 2015; Sztybor and Rasmussen, 2017a) is the only directly dated paleo-methane seepage episode from Vestnesa Ridge. Its age (17.7-16.7 ka BP; Figs. 7; 8) indicates the shell bed persisted for a period of approximately 1,000 years during HE 1 (18-15 ka BP; Ambrose et al., 2015; Figs. 7; 8). The species composition is typical for bivalves and gastropods that lived partially burrowed at the sediment surface (Ambrose et al., 2015). Furthermore, the mineral composition of the MDAC nodules found within the shell bed in cores HH-13-203 (Fig. 5b) and HH-12-211 (Fig. 6a) suggests that the chemosynthetic bivalve community colonised the former sediment surface. The shell bed occurs in two different pockmarks spaced approximately 2 km apart, but is absent in the area between those pockmarks. The similar species composition and concurring ages suggest the shell bed represents the

same biological community. During HE 1 chemosynthetic bivalves recovered from the two different pockmarks document a common methane seepage phase suggesting a regional event, or the same subsurface conduit supplied both pockmarks.

Ongoing methane seepage at Vestnesa Ridge is under regular observation since 2008 (Hustoft et al., 2009; Bünz et al., 2012; Panieri et al., 2017b) and seems to be persistent for nearly a decade. At the western Svalbard margin and Vestnesa Ridge, erosion or non-deposition throughout the Holocene exposes sediments older than 10-9 ka at the seafloor (Elverhøi et al., 1995; Howe et al., 2008) and the present-day SMTZ commonly occurs in host sediments up to 13.4 ka old (section 4.3; Figs. 5; 6). We suggest that geological evidence for past methane seepage in post-glacial sediments, such as negative foraminiferal $\delta^{13}C$ excursions, MDAC nodules, and elevated Sr/Ti elemental ratios, do not necessarily correspond to the host sediment age. Those proxies may in reality represent the present-day SMTZ, or SMTZ shoaling in ancient host sediment due to changes in methane fluxes.

When other proxies are absent, our data do not reveal if all methane was consumed at the SMTZ and resulted in early diagenesis near the seafloor, or if a fraction of the methane surpassed the SMTZ, left the seafloor sediments, and eventually entered the bottom water. Because of their diagenetic nature, sedimentary proxies indicating paleo-SMTZs may not always correspond to paleo-methane seepage, but instead may propose dynamic vertical SMTZ migration and subseafloor methane cycling in ancient host sediments. Susbseafloor diagenesis may indicate calm periods of the fluid flow system and subsequent reactivation.

From the Lunde and Lomvi pockmarks, high spatial heterogeneity of seepage with diffuse and focused fluid flow has been described by Panieri et al. (2017b). Thus, observations of subseafloor methane enrichment and SMTZ shoaling may suggest weaker, diffuse fluid flow while evidence of real seafloor methane seepage from the shell bed may be analogue to stronger, focused fluid flow that is currently occurring in gas flares emanating from pits within the Lunde and Lomvi pockmarks.

4.5 Seepage drivers

Two hypotheses compete about the governing controls on seepage timing at Vestnesa Ridge: 1) Changes in the oceanic thermal regime have the ability to drive gas hydrate dissociation (Sztybor and Rasmussen 2017a); and 2) changes in the lithospheric stress regime may result in increased tectonic activity, reactivation of pre-existing faults and fractures, and thus initiating gas migration and seafloor methane seepage (Ambrose et al., 2015; Consolaro et al., 2015; Plaza-Faverola et al., 2015).

4.5.1 Seepage in response to bottom water temperature (BWT) increase

During the LGM, BWTs in the Arctic Ocean and the Nordic Seas have been 2-3°C warmer than Holocene and modern temperatures (Cronin et al., 2012; Thornalley et al., 2015). After SBIS disintegration, the BWT along the western Svalbard margin remained warm due to northward advection of Atlantic water as a subsurface current below the surficial cold and low salinity water, and reached maximum temperatures during the Bølling-Allerød interstadials (Rasmussen and Thomsen, 2004; Rasmussen et al., 2007; Ślubowska-Woldengen et al., 2007), which is documented by the occurrence of warm-water benthonic foraminiferal species (Rasmussen et al., 2007; Sztybor and Rasmussen, 2017a; Consolaro et al. accepted manuscript). More recently, Sztybor and Rasmussen (2017a) have suggested that during HE 1 Atlantic subsurface and bottom waters at Vestnesa Ridge had reached their maximum temperatures over the past 43 ka. This is based on the abundance of warm-water benthonic foraminifera and *Vesicomyidae* bivalves, the latter are today most abundant at low latitudes between 30°S and 30°N, and nearly absent at latitudes beyond 60° (Krylova and Sahling, 2010; Hansen et al., 2017).

Sztybor and Rasmussen (2017a) hypothesize that *Vesicomyidae* may have benefited from warmer BWT at Vestnesa Ridge during HE 1 and propose that, in addition to elevated methane concentrations, warmer BWT during HE 1 may have been a controlling factor on the occurrence of the shell bed formed at 17 ka BP.

Even if the available heat energy from elevated BWT during the LGM was adequate to warm up the sediment and dissociate a sufficient amount of gas hydrate at Vestnesa Ridge, heat propagation

691 through sediments is generally slow (Xu et al., 2001; Taylor et al., 2005; O´Connor et al., 2010; Darnell
692 and Flemings, 2015). Moreover, gas hydrate decomposition is an endothermic process and hence
693 slows down heat propagation in sediments (Torres and Bohrmann, 2006). Furthermore,
694 chemosynthetic bivalve communities are known to colonize seeps with intermediate to intense, slow
695 and persistent fluid flow over time scales of decades to centuries (Callender and Powell, 2000; Kiel,
696 2010; Bowden et al., 2013; Levin et al., 2016). Therefore, we do not support the hypothesis that BWT
697 increase during HE 1 was the main reason why methane seepage occurred and chemosynthetic
698 organisms colonised the seep.
699

700 *4.5.2 Effects of glacio-isostatic adjustment (GIA) on methane seepage*
701 The fact that recorded seepage events at Vestnesa Ridge are restricted to neither glacial nor
702 interglacial periods suggests that the drivers controlling seepage activity are not strictly related to
703 climatic and/or oceanographic variations but may involve other Earth system processes. Ambrose et
704 al. (2015) hypothesize that the chemosynthetic bivalves of the shell bed were associated with tectonic
705 instabilities such as faulting and fracturing leading to a 1000 years long seepage interval at Vestnesa
706 Ridge. In contrast, Consolaro et al. (2015) suggested the combined effect of sea level rise, elevated
707 sedimentation rate and isostatic rebound as important factor for seepage modulations at Vestnesa
708 Ridge.
709 In particular, glacio-isostatic adjustment (GIA) accompanying variations in SBIS extent emerges as an
710 alternative explanation for SMTZ migration and seepage on Vestnesa Ridge. Glacio-isostatic
711 adjustment is the viscoelastic response of the Earth`s surface to loading and unloading of the crust due
712 to ice sheet dynamics, and causes two main types of stresses. Vertical stresses occur due to crustal
713 subsidence and displacement of viscous mantle material to the periphery of the load centre during ice
714 sheet growth (Lambeck and Chappell, 2001; Peltier, 2001; Whitehouse 2009; Lund, 2015). The
715 horizontal flexure of the Earth`s crust and increases in the pore fluid pressure cause fault instabilities
716 and opening of fractures (Hutri et al., 2007; Lund et al., 2011). In addition, the rebound stress (i.e.

717 during deglaciation) can be strong enough to cause slip on faults that are close to failure due to
718 background regional stresses (e.g. Lund et al., 2011 and references therein).
719 Linear high permeability conduits such as neotectonic faults and fractures have long been recognised
720 as pathways for fluid migration that is commonly initiated by changes in pore water pressure and/or
721 increased seismicity (e.g. Milkov, 2000; Revil, 2002; Jonsson et al., 2003; Ho et al. 2010; Dupre et al.,
722 2015; Franek et al. accepted manuscript). Additionally, a modelling study performed by Klusman and
723 Saeed (1996) suggests gaseous hydrocarbons preferably migrate vertically as buoyant microbubbles
724 along fault systems. For the western Svalbard continental margin, the chemical characteristics of
725 gaseous hydrocarbons suggest vertical migration along re-activated fault systems (Knies et al., 2004).
726 This is consistent with a study from Mau et al. (2017) who report a significant number of gas discharge
727 sites between 74 and 79°N at the western Svalbard continental margin where faults such as the
728 Hornsund Fracture Zone intersect the seafloor and underlying rock. Although Vestnesa Ridge is located
729 a few kilometres to the west of the shelf break of the western Svalbard continental margin on oceanic
730 crust and in 1200 to 1300m water depth, GIA at the SBIS periphery could have sparked the re-activation
731 of pre-existing faults and fractures at Vestnesa Ridge. The opening of fluid migration pathways may
732 have facilitated subseafloor methane enrichment that was leading to shoaling of the SMTZ, shallow
733 subseafloor diagenesis, and/or seafloor methane seepage.
734 Sediments along the ridge have been exposed to complex tectonism (e.g. Crane et al., 2001). Plaza-
735 Faverola et al. (2015) documented sub-seafloor faults and fractures associated with pockmarks on
736 both, the active eastern segment and the western inactive segment. Based on differences in the
737 faulting pattern and fault orientation on the eastern compared to the western Vestnesa Ridge
738 segment, the authors postulated that tectonic stress variations along the ridge may control seepage
739 activity. The striking differences between the $\delta^{13}C$ curves from the core on the north-western Vestnesa
740 Ridge segment (JM10-330, Fig. 4b) and cores from active pockmarks towards the south-east support
741 the notion of different regional response of Vestnesa Ridge to tectonic processes.
742

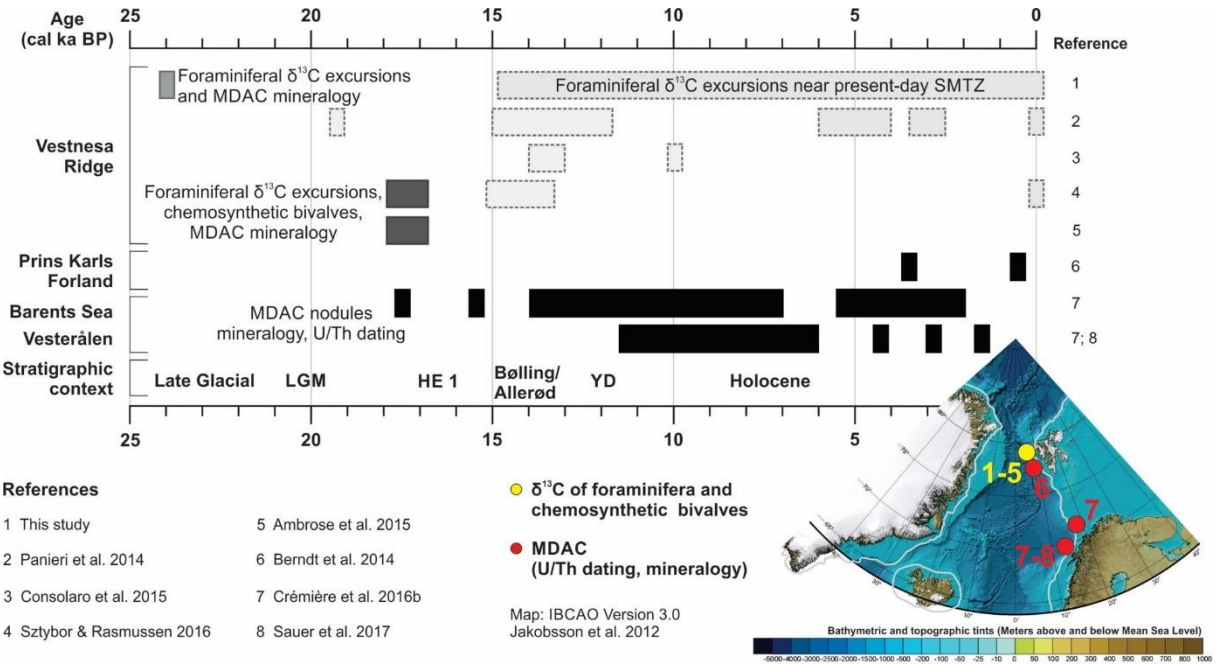

Fig. 8. Records of methane seepage since the LGM in the Nordic Seas. Light grey box – foraminiferal $\delta^{13}C$ excursions and MDAC mineralogy in Event 1 sediments. Light grey boxes with dashed line – foraminiferal $\delta^{13}C$ excursions approximately corresponding with the present-day SMTZ position and assumed vertical SMTZ migration. Dark grey boxes – chemosynthetic bivalves of the shell bed, foraminiferal $\delta^{13}C$ excursions and MDAC mineralogy. Black boxes – U/Th geochronology and mineralogy of MDAC nodules. Bathymetry from IBCAO 3.0 (Jakobsson et al., 2012). Grey line delineates the LGM extent of the SBIS, Iceland and Greenland Ice Sheets according to Patton et al. (2015).

Direct evidence confirms methane seepage during SBIS retreat and throughout the Holocene in the Nordic Seas (Fig. 8). Seafloor methane seepage in the south-western Barents Sea Shelf is well documented in MDAC crusts that formed from 17.5 ka BP on with the majority of U/Th dates culminating between 14 and 7 ka BP and 2 ka BP being the youngest ages (Crémière et al., 2016b). At the Vesterålen margin offshore northern Norway, MDAC reveal methane seepage between 11.5 and 6 ka BP (Crémière et al., 2016b) in response to isostatic rebound, pressure release, gas migration along faults, and bottom water warming after disintegration of the Fennoscandian Ice Sheet. Methane seepage following ice sheet retreat appears to be a phenomenon that is not limited to the Northern

761 Hemisphere. Römer et al. (2014) discovered an extensive methane seep area on the northern shelf
762 offshore South Georgia, Antarctica. Radial fjords and cross-shelf troughs approaching the shelf break
763 indicate that the island was covered by an extensive ice sheet (Graham et al., 2017). Deglaciation of
764 the shelf edge occurred around 19 ka BP (Graham et al., 2017) while the coast became ice-free around
765 12 ka BP (Bentley et al., 2007). Thus, the subseafloor methane enrichment event during the LGM and
766 the paleo-seepage event documented by the shell bed during HE1 are likely to be in close relationship
767 with SBIS maximum extent and disintegration in north-western Svalbard.
768 After deglaciation, it takes many thousand years to reach isostatic equilibrium through delayed crustal
769 rebound during which seismicity slowly declines. Glacio-isostatic adjustments are lasting longer than
770 the impact of an ice sheet and thus may cause seismic and tectonic activity initiating fluid flow and
771 seabed seepage long after an ice sheet has vanished. This is documented on Svalbard in raised
772 shorelines throughout the Holocene (Forman et al., 1990; 2004) and earthquake activity along the
773 Norwegian continental margin (Fjeldskaar et al., 2000; Lambeck and Chappell, 2001; Bungum et al.,
774 2005; Lund 2015; Lee, 2009; Olesen et al., 2013). Sauer et al. (2017) obtain ages of 4.4-1.6 ka from
775 seafloor MDAC crusts that were found at the Vesterålen margin offshore northern Norway. The
776 authors suggest episodes of increased seismicity at the Lofoten-Vesterålen area are due to remaining
777 GIA movements, that triggered earthquake activity and facilitated methane flux and MDAC
778 precipitation. Furthermore, U/Th-dated MDAC crusts show that methane seepage occurred until 2000
779 years ago at the south-western Barents Sea, and has been ongoing for at least 3000 years offshore
780 western Svalbard where MDAC also precipitated within the past 500 years (Berndt et al., 2014;
781 Crémière et al., 2016b).
782 Although our dataset does not always allow differentiating between shallow subseafloor diagenesis in
783 Early Holocene host sediment and real paleo-seepage episodes, we cannot exclude seepage during the
784 Holocene on Vestnesa Ridge either. Some of the paleo-SMTZs in our records may indeed capture
785 seepage episodes with similar timing as it was observed in MDACs in the Barents Sea and at the
786 Norwegian continental margin.

Glacial isostatic adjustment is an integral component of the Earth system and acts on geological time scales. Compelling evidence complements the hypothesis that GIA sparked tectonic activity and fault re-activation also offshore western Svalbard, may have enabled fluid migration, subseafloor methane enrichment, and seafloor methane seepage at Vestnesa Ridge during SBIS disintegration. Diagenetically altered foraminiferal tests, MDAC, sediment geochemical records, and chemosynthetic fauna suggests that shallow subseafloor diagenesis and seafloor methane seepage at Vestnesa Ridge may respond to long-term changes in Earth system processes rather than to climate change in human time scales (Dickens, 2003; Hong et al., 2017).

5 Conclusions

We establish a convincing stratigraphic framework for the sediments along Vestnesa Ridge using the existing stratigraphic marker horizons defined for the western Svalbard margin between 76 to 80°N. Our data are consistent with the $\delta^{18}O$ stratigraphy for planktonic foraminifera from the north-western Svalbard margin during the Last Glacial Maximum (LGM), deglaciation and Early Holocene and thus provide an important chronological framework for stratigraphic correlation and interpretation of methane-related diagenetic processes.

Shallow subseafloor diagenesis and seafloor seepage cover the complete time span since the LGM and disintegration of the Svalbard-Barents Sea Ice Sheet (SBIS), and are documented in multiple proxies (negative foraminiferal $\delta^{13}C$ excursions, MDAC nodules, elevated Sr/Ti elemental ratios, chemosynthetic bivalves) preserved in the sedimentary record. Seafloor methane seepage occurred during the LGM (24-23.5 ka BP) and Heinrich Event 1 (HE 1, 17.7-16.7 ka BP).

Sedimentary proxies indicating paleo-SMTZs do not always correspond to seafloor methane seepage but instead may indicate shallow subseafloor diagenetic methane cycling and SMTZ shoaling. Such paleo-SMTZ`s may be formed in the subsurface and do not necessarily correspond to the host sediment age. Indications of methane seepage other than during LGM, HE 1 and at the

present-day SMTZ possibly represent weaker methane flux since the sediment deposition until today.

Although the influence of elevated bottom water temperatures on seafloor methane seepage cannot be excluded, we consider glacio-isostatic adjustments as most important factor controlling past and ongoing methane seepage and diagenetic methane cycling on Vestnesa Ridge. The build-up and disintegration of major ice sheets is accompanied by crustal isostatic adjustments and increased seismicity. Glacio-isostatic adjustments may have triggered the re-activation of faults and fractures at Vestnesa Ridge and thus could have provided fluid migration pathways.

6 Acknowledgements

This work was supported by the Research Council of Norway through its Centre of Excellence funding scheme for CAGE, project number 223259 and partially by the NORCRUST project [grant number 255150]. Parts of the isotopic analyses were supported by the PNRA Project FORMAT. We thank the captain, crewmembers and scientific team of *R/V Helmer Hanssen* for their contribution during the research cruises CAGE-2013 and CAGE-2014. We are indebted to Stefan Bünz who acquired 3D seismic data from the Vestnesa Ridge and facilitated bathymetry maps for the study area. AS obtained a travel grant from the Norwegian Research School in Climate Dynamics (ResClim). The manuscript benefited from editing and language correction by Monica Winsborrow and Hanne-Kristin Paulsen.